https://doi.org/10.1016/j.optcom.2018.07.047

Optical and Quantum Models of Resonant Optical Tunneling Effect

AOQUN JIAN,[1,2] GANG BAI, [1,2] YANXIA CUI,[2,3] CHONGGUANG WEI,[1,2]

XIN LIU,[2,3] QIANWU ZHANG,[4] SHENGBO SANG,[1,2,6] AND XUMING ZHANG[5,7]

[1] *MicroNano System Research Center, Taiyuan University of Technology, Taiyuan 030024, China;*
[2] *Key Laboratory of Advanced Transducers and Intelligent Control System, Shanxi Province and Ministry of Education, Taiyuan 030024, China*
[3] *College of Physics and Optoelectronics, Taiyuan University of Technology, Taiyuan 030024, China*
[4] *Key Laboratory of Specialty Fiber Optics and Optical Access Networks, Shanghai University, Shanghai 200072, China*
[5] *Department of Applied Physics, Hong Kong Polytechnic University, Hung Hom, Kowloon, Hong Kong, China*
[6] sunboa-sang@tyut.edu.cn
[7] xuming.zhang@polyu.edu.hk

Abstract: Resonant optical tunneling effect (ROTE) is a special phenomenon that light can fully go through the seemingly impenetrable optical structure. It is a prominent example to study the analogy of wave optics and quantum physics. Previous theoretical work mostly focused on the optical modeling of transmission spectrum using the transfer matrix method (TMM), but put little effort in the quantum model. This paper advances the optical modeling by using the finite-difference time-domain method (FDTD) to simulate the electric field distribution and by using the plane wave expansion (PWE) to predict the optical bandgap. Moreover, we present the first analytical quantum model of the ROTE and further derive a direct expression of the transmission peak positions. This expression cannot be derived by the optical models, but its predicted peak positions match the optical modeling results using the FDTD, the PWE and the TMM. This well demonstrates the merit of the quantum analogy for analyzing the optical systems. This work may inspire the transplantation of the established ideas and designs in the quantum field into the optical field to create new optical and photonic devices.

OCIS codes: (260.5740) Resonance; (000.1600) Classical and quantum physics.

References and links

1. S. Zhu, A. W. Yu, D. Hawley, and R. Roy, "Frustrated total internal reflection: A demonstration and review," Amer. J. Phys., **54**(7), 601–607(1986).
2. F. de Fornel, Evanescent Waves: From Newtonian Optics to Atomic Optics, (Springer, 2005), Chap.1.
3. A. B.Shvartsburg, "Tunneling of electromagnetic waves: paradoxes and prospects," Phys.-Usp., **50**(1), 37-51(2007).
4. C. Buisset, Y. Rabbia, T. Lepine, M. A. Alagao, E. Ducrot, S. Poshyachinda and B. Soonthornthum , "Study of a coronagraphic mask using evanescent waves," Opt. Express, **25**(7), 7273-7287(2017).
5. Y. Chen, Y. Ban, Q. B. Zhu, and X. Chen, "Graphene-assisted resonant transmission and enhanced Goos–Hänchen shift in a frustrated total internal reflection configuration," Opt. Lett., **41**(19), 4468-4471(2016).
6. S. Hayashi, H. Kurokawa and H. Oga, "Observation of resonant photon tunneling in photonic double barrier structures," Opt. Rev., **6**(3), 204-210(1999).
7. A. Q. Jian, X. M. Zhang, "Resonant optical tunneling effect: recent progress in modeling and applications," IEEE J. Sel. Top. Quant, **19**(3), 9000310-9000310(2013).
8. S. Longhi, "Resonant tunneling in frustrated total internal reflection," Opt. Lett., **30**(20), 2781-2783(2005).
9. A. Melnyk, M. H. Bitarafan, T. W. Allen, and R. G. DeCorby, "Air gap resonant tunneling bandpass filter and polarizer," Opt. Lett., **41**(8), 1845-1848 (2016).
10. A. G. Krause, M. Winger, T. D. Blasius, Q. Lin and O. Painter, "A high-resolution microchip optomechanical accelerometer," Nat. Photonics, **6**(11), 768-772(2012).

11. M. A. Komatsu, K. Saitoh and M. Koshiba, "Design of miniaturized silicon wire and slot waveguide polarization splitter based on a resonant tunneling," Opt. Express, **17**(21), 19225-19234(2009).
12. N. Yamamoto, K. Akahane, and S.-I. Gozu, "All-optical control of the resonant-photon tunneling effect observed in GaAs/AlGaAs multilayered structures containing quantum dots," Appl. Phys. Lett., **87**(23), 231119-1–231119-3(2005).
13. W. M. Zhu, T. Zhong, A. Q. Liu, X. M. Zhang and M. Yu, "Micromachined optical well structure for thermo-optic switching," Appl. Phys. Lett., **91**(26), 261106(2007).
14. A. Q. Jian, X. M. Zhang, W. M. Zhu, and M. Yu, "Optofluidic refractometer using resonant optical tunneling effect," Biomicrofluidics, **4**(4), 043008(2010).
15. A. Q. Jian, X. M. Zhang, W. M. Zhu, and A. Q. Liu, "Liquid refractive index sensors using resonant optical tunneling effect for ultra-high sensitivity," Sens. Actuators A, **169**(2), 347–351(2011).
16. S. Longhi, "Quantum-optical analogies using photonic structures," Laser Photonics Rev., **3**(3), 243-261(2009).
17. R. Y. Chiao and A. M. Steinberg, "Tunneling times and superluminality," Prog. Optics, **37**, 345–405(1997).
18. A. M. Steinberg, P. G. Kwiat, and R. Y. Chiao, "Measurements of single photon tunneling time," Phys. Rev. Lett., **71**(5), 708–711(1993).
19. A. M. Steinberg and R. Y. Chiao, "Subfemtosecond determination of transmission delay times for a dielectric mirror (photonic band gap) as a function of the angle incidence," Phys. Rev. A, **51**(5), 3525–3528(1995).
20. A. M. Steinberg and R. Y. Chiao, "Tunneling delay times in one and two dimensions," Phys. Rev. A, **49**(5), 3283–3295(1994).
21. R. Y. Chiao, P.G. Kwiat, and A. M. Steinberg, "Analogies between electron and photon tunneling," Physica B, **175**(1-3), 257–262(1991).
22. B. Lee and W. Lee, "TM-polarization photon tunneling phase time in a frustrated-total-internal-reflection structure," J. Opt. Soc. Amer. B, **14**(4), 777–781(1996).
23. J. D. Joannopoulos, S. G. Johnson, J. N. Winn and R. D. Meade, Photonic Crystals Molding the Flow of Light (Princeton University Press, 2007), Chap. 3.
24. J. M. Guerra, "Photon tunneling microscopy," Appl. Opt., **29**(26), 3741–3752(1990).
25. S. Takahashi, T. Fujimoto, K. Kato, and I. Kojima, "High-resolution photon scanning tunneling microscope," Nanotechnology, **8**(3A), A54–A57(1997).
26. P. S. Carney, R. A. Frazin, S. I. Bozhevolnyi, V. S. Volkov, A. Boltasseva, and J. C. Schotland, "A computational lens for the near-field," Phys. Rev. Lett., **92**(16), 163903-1–163903-4(2004).
27. D. K. Ferry, Quantum Mechanics: An Introduction for Device Physicists and Electrical Engineers (Institute of Physics Pub, 2001), Chap. 3.

1. Introduction

Photonic tunneling, which represents a special phenomenon that lightwave can tunnel through classically impenetrable optical structures, has been a key topic of intense scrutiny over decades [1]-[5]. As an unique effect combining both the photonic tunneling and the resonance phenomenon, resonant optical tunneling effect (ROTE), has arisen extensive theoretical [6]-[8] and experimental attentions in recent years [9]-[11]. As shown in Fig. 1, the ROTE structure basically consists of 5 layers with a high–low–high–low–high refractive index (RI) distribution. Total reflection is formed at the initial incident interface of high–low RI media. With some distinct advantages, the ROTE exhibits potential for application in high-performance devices such as optical switches [12], [13] and refractive index sensors [14], [15].

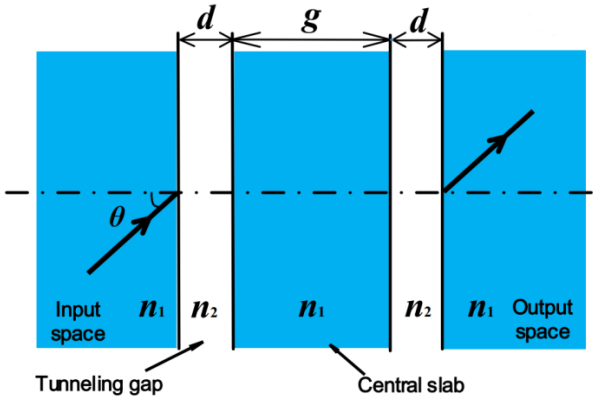

Fig. 1. Schematic graph of the ROTE structure.

In a broad category, research on the ROTE is part of continuous efforts to investigate the analogies between wave optics and quantum mechanics, which have provided great opportunities to transfer new ideas, concepts, and methods among apparently different physical fields [16]. Such analogies benefit both optics and quantum mechanics in many aspects. For example, the analogy of quantum physics and optics offers a feasible approach to visualize ultrafast phenomena in the quantum field. Several basic physical properties of electron tunneling, such as tunneling time, superluminal effect and phase delay, are explored using the photon tunneling model [17]-[22]. In the 1990s, Chiao et al. [21] and Lee et al. [22] applied the optical barrier structure to study the fundamental properties of tunneling, such as tunneling time, phase time and post-tunneling positions.

Meanwhile, the quantum analogy of optics provides a refreshed view to analyze complex optical systems with unprecedented functions. The photonic crystal borrows the idea of electronic band gap when electrons move in the crystal lattice and generates the optical band gap for photons [23]. Regarded as a classical theory, this concept vividly and precisely describes the features of light propagation in periodic dielectric structures and leads to a flourishing research area of fundamental and practical interest (e.g., photonic bandgap crystals). Furthermore, inspired by the scanning tunneling microscopy, the photon tunneling microscopy with ultrahigh spatial resolution has been developed to use an optical tip to tunnel photons for 3-D topographic imaging [24]–[26].

On the basis of the analogy, the quantum interpretation of ROTE is introduced in the author's previous review [7]. However, the detailed analysis of the physical mechanism of ROTE remains unavailable. In the present study, the physical mechanism of ROTE can be examined from two origins: the optics interpretation and the quantum interpretation. The former originates from the wave nature of light and regards the ROTE as the propagation of lightwave through a multilayered film. The latter is derived based on the particle nature of light and treats the ROTE as the electrons going through a quantum well, which has been widely used for resonant tunneling diodes. Fundamentally, the optics interpretation is based on the Maxwell's equations, whereas the quantum interpretation is based on the time-independent Schrödinger equation. This is the first time that the corresponding analogy contributes to the design/characterization of applied photonic devices.

2. Optics interpretation

In this section, the ROTE is regarded as a multilayer system and analyzed based on Maxwell's equations. Compared with the quantum interpretation, the optics interpretation analyzes ROTE from a classical perspective. The physical mechanism of ROTE is presented in detail by using various simulation methods. The distinct characteristics of ROTE can also be revealed by comparing the ROTE with other similar optical models, such as the photonic crystals and Fabry–Pérot etalons. In the classical interpretation, the electromagnetic field distribution of the ROTE structure is presented using the finite-difference time-domain (FDTD) simulation. The existence of the ROTE mode is verified in accordance with the results of plane wave expansion (PWE).

2.1 FDTD study of ROTE

The simulation model of the ROTE structure is shown in Fig. 2 (Lumerical FDTD). In the ROTE structure, the medium of the tunneling gap (low RI layers) is set as air, whereas that of others (high RI layers) is silicon. Thus, the materials from the input to the output space consist of silicon–air–silicon–air–silicon. The values for the basic structural parameters of the model are listed in Table 1. To form the total reflection, the angle θ of the incident light is set to be 18.0016°, which is l degree larger than the critical angle (17.0016°). As linearly polarized light emitted from the light source passes through the integrated ROTE structure, the power monitor collects the transmission power in the output space. Given the extremely

low absorption of silicon in the near-infrared band, the simulations/calculations conducted in the study neglect the absorption of the materials, and thus focus only on the structural characteristics.

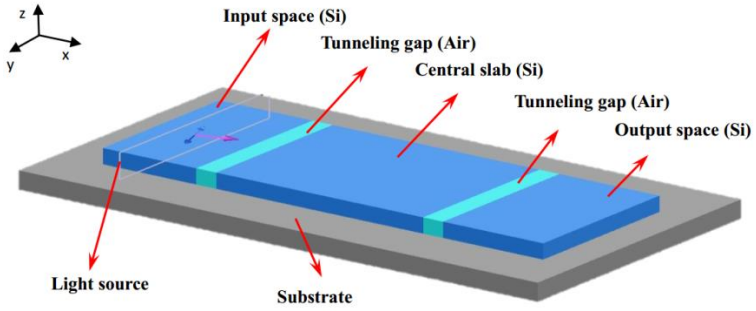

Fig. 2. Optical model of ROTE set up in FDTD simulation.

Table 1. Parameters of the ROTE structure

Parameter	Symbol	Values	
		S-pol	P-pol
Incident angle	θ	18.0016°	18.0016°
Width of central slab	g	15.5 μm	15.5 μm
RI of input and output space	n_1	3.420	3.420
RI of central slab	n_1	3.420	3.420
RI of tunneling gap	n_2	1.000	1.000
Width of tunneling gap	d	1 μm	1 μm

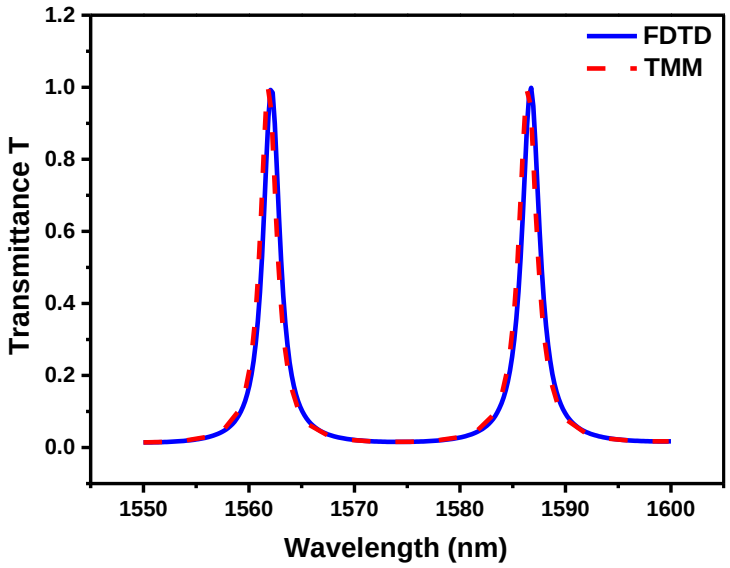

Fig. 3. Transmission spectrum of ROTE obtained by TMM and FDTD methods for P-polarization.

With reference to the structure above, Fig. 3 shows the transmission spectrum of the ROTE structure for P-polarization obtained by both the FDTD simulation and the calculation using the transfer matrix method (TMM) (details shown in Supplementary). These transmission curves almost overlap, verifying the correctness of the FDTD simulation. Sharp

transmission peaks are obtained at the wavelengths of 1562.05 and 1586.75 nm, the transmittance of which achieve 1.0 (100%). This finding indicates that the incident light can completely pass through even though the total reflection occurs at the incident interface. This is one of the distinctive features of ROTE as compared to the other effects using the evanescent waves (e.g., frustrated total internal reflection), whose transmittance is mostly < 100%.

To further analyze the distribution of electric field propagation, incident wavelengths with different transmissions T (T = 1, 0.52, and 0.015) are selected to simulate the electric field mode profiles. The 2D electric field distributions of the incident plane along the propagation direction and the corresponding profile curves are plotted in Fig. 4. The blue and red dotted boxes represent the spatial range of the tunneling gap d (X-axis: 0–1μm, 16.5–17.5μm) and the central slab g (X-axis: 1–16.5μm), respectively. In the case of high transmission (Fig. 4(a) and (d)), the evanescent field of the first tunneling gap appears enhanced with an increase in the propagation depth, which varies from the classical evanescent wave; the amplitude of evanescent wave "decays" exponentially into the low RI layer (i.e., the first tunneling gap in ROTE).

Subsequently, the evanescent field mode extends across the boundary of the high-RI medium layer and achieves a localized enhanced mode of electric field in this layer. The enhanced electric fields are then coupled through the second tunneling gap as the decay field. In particular, the electric field presents a highly axial symmetric distribution along the ROTE structure. However, as shown in Figs. 4(e) and 4(f), the electric field distribution of the tunneling gap is not symmetrical for non-resonant wavelengths. In Fig. 4(b), the evanescent field decays first and then rises in the first tunneling gap, and two evanescent decay fields are found in the two tunneling gaps in Figs. 4(c) and 4(f). Compared with Figs. 4(a)–4(c), although a different transmittances T occurs at a specific wavelength, all transmittances can form a standing wave in the central slab zone (range in the X-axis: 1–15.5μm) because of the interference. Fig. 4(g) summarizes the amplitudes of standing waves with different transmittances. With an increase in the transmission T, the amplitude grows significantly; the maximum value of 2.51 can be obtained when T = 1. In addition, the standing waves on the left side of the first tunneling gap (the range in X-axis: -1–0μm) in Figs. 4(e) and 4(f) are attributable to the interference between the incident light (position of the X-axis: -1μm) and the reflected light.

Polarization dependence of the ROTE is investigated. Fig. 5 describes the transmission spectra (a) and electric field distribution of S- and P-pol. incidence with the tunneling gap d = 0.5 μm. The result indicates that the transmission spike of S-pol. is much sharper than that of P-pol., and the resonant wavelength shifts occur in different polarization states.

The intensity pattern for both polarization states presents markedly linear symmetry within the ROTE structure, which consists of the evanescent wave (occurring in the tunneling gaps) and the standing waves in the central slab. The field amplitude of P-pol. (1.14) is considerably smaller than that of S-pol. (7.16). In addition, compared with the two curves in Fig. 5(b), the electric field for P-pol. presents a discontinuous change at the interface of the input space and the tunneling gap (X-axis: 0 μm) in contrast to the continuum of S-pol. The reason is that the propagation of incident polarized light meets the boundary conditions for an ideal medium interface; the tangential component of the electric field E and the normal component of the electric displacement vector D keeps continuous at the interface, respectively.

Figs. 4 and 5, regardless of polarization states, indicate that owing to the interference, the electric field is greatly enhanced in the central slab of the ROTE structure in the cases of incidence with a specific wavelength (T = 1); that is, resonance occurs (like in Fabry–Pérot etalons, whisper galley mode ring resonators, etc.). In the resonance state, the double-length of the central slab is the integral multiple of the wavelength of the standing wave located in the central slab (Fig. 5(b)). The higher electric-field intensity indicates a greater accumulation

of energy in the resonator; thus, the corresponding ROTE peak in the output spectrum has a higher Q value.

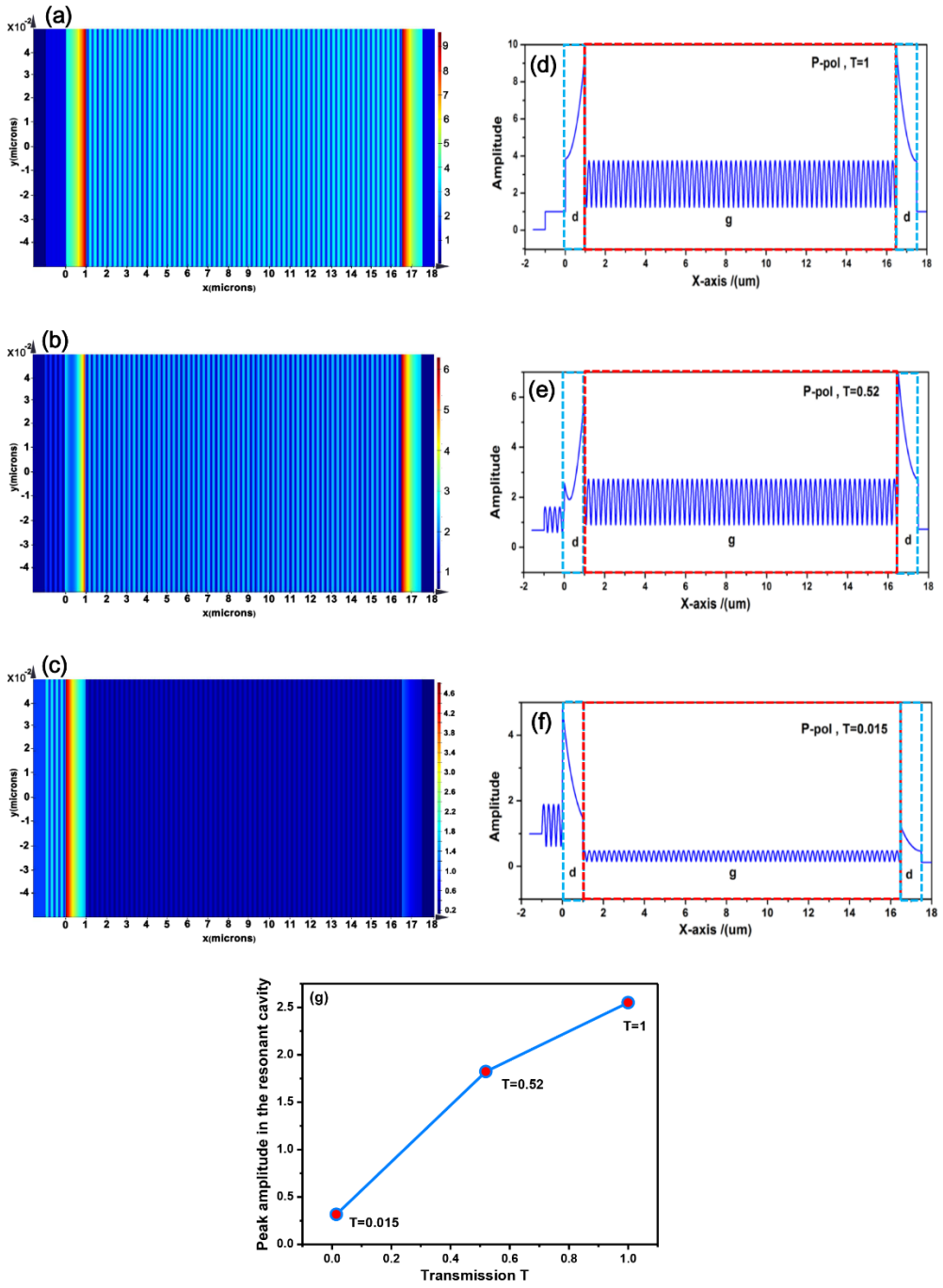

Fig. 4. Electric-filed distribution and its profile of ROTE structure in different transmission states: (a) and (d) T = 1; (b) and (e) T = 0.52; (c) and (f) T = 0.015. (g) The standing-wave amplitude in the central slab layer of ROTE structure with different transmittances.

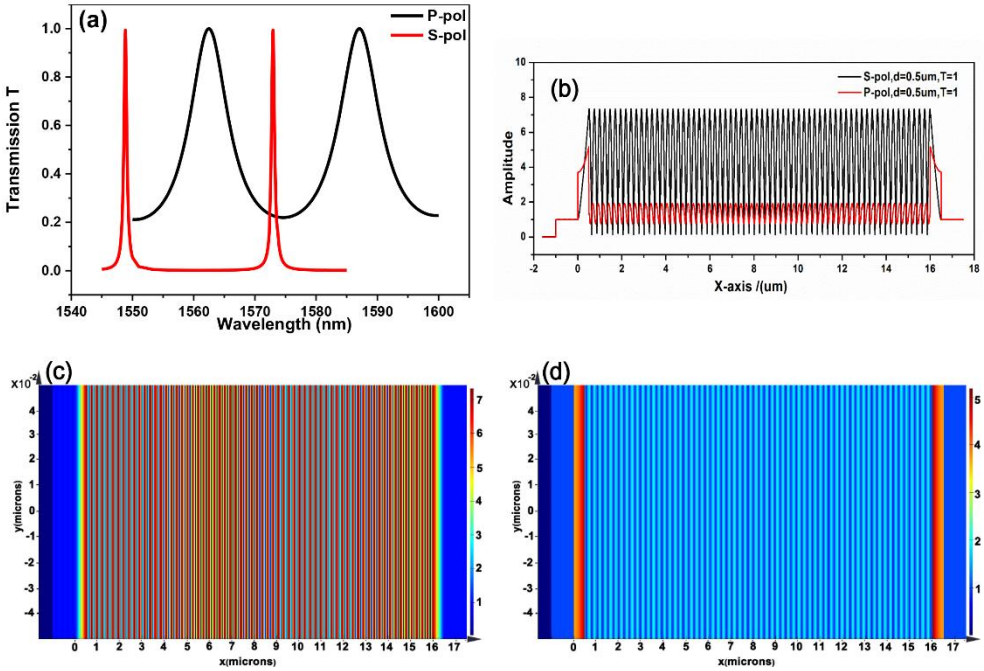

Fig. 5. Transmission spectra of the ROTE structure in S-polarization and P-polarization obtained by FDTD simulations (a); Profile of electric-field distribution along the *X*-axis direction (b); 2D plane graph of electric-field distribution for S-polarization and P-polarization at the resonant wavelength (c) and (d).

2.2 Plane Wave Expansion

In order to explore of the origin of the ROTE, it is a straightforward way to consider the ROTE model as a part of multilayer structure, which includes two layers with two different RIs alternating with each other, as shown in Fig. 6(a).

Fig. 6(b) shows the band structure diagram of off-axis propagation of one dimensional photonic crystal corresponding to the ROTE model (the same as the model in the Table.1), which is solved by plane wave expansion (PWE). The slope of the straight line passing the origin varies with the angle of incidence, as shown in Eq. (1)

$$k = \frac{1}{n \sin \theta} \tag{1}$$

where k is the slope of the straight line, and n and θ denote the RI and the incidence angle in the same layer, respectively.

In Figs. 6(b) and (c), the vertical ordinate represents the normalized frequency $\frac{\omega a}{2\pi c} = \frac{a}{\lambda}$, where ω is the angular frequency, c is the speed of light, λ is the wavelength, and a is the lattice constant. The horizontal coordinate is the wave vector off-axis ky. The red and blue lines correspond to the center and boundary of the Brillouin zone, respectively. Thus the gaps between adjacent curves with the same color are regarded as band gaps. Fig. 6(c) is the close-up view of interested range of the band structure diagram (the wavelength ranges from 1500–1600 nm). According to Eq. (1), the black line is shown in the Figure 6(b) and (c), which corresponds to the incident angle 18.0016°.

The transformed band structure based on the PWE (red line), together with the calculated transmission spectrum from the TMM (black line) are is compared in Fig. 6(d). To clearly

illustrate the band gaps in the transmission spectrum and to compare them with the results obtained using the TMM, the transmittance of the wavelength range corresponding to the band gap is assumed to be 0, whereas that of other ranges is 1. As observed, all transmission peaks stand at the center of permitted bands, whereas all troughs are located at the center of the band gap. This observation indicates that ROTE peaks originate from the eigen modes of the binary mutilayer structure.

Although the PWE method successfully explains the origination of the ROTE, it is noted that the ROTE structure is quite different from the general photonic crystal structure. The reasons lie in as follows:

First, the number of uniform units of photonic crystal is very large (normally over 10), whereas the ROTE system is quite a simple structure (consisting of 5 layers in total) but performs extremely well for some specific applications [14]. Moreover, the ROTE structure emphasizes the condition that the incident angle of the input light should exceed the critical angle, which is a key factor for obtaining a unique feature of the ultrahigh Q transmission peak. Although the total internal reflection effect is involved in the photonic crystal (evanescent mode), the connection between the incident condition and the characteristics of the transmission peak is rarely discussed. Finally, the analogous relationship between the optics and the quantum mechanism provides a great opportunity for ROTE, which has a distinct physical mechanism combining the tunneling effect and the resonance phenomenon, thus offering potential contributions to the field of quantum mechanics. More details can be found in the next section.

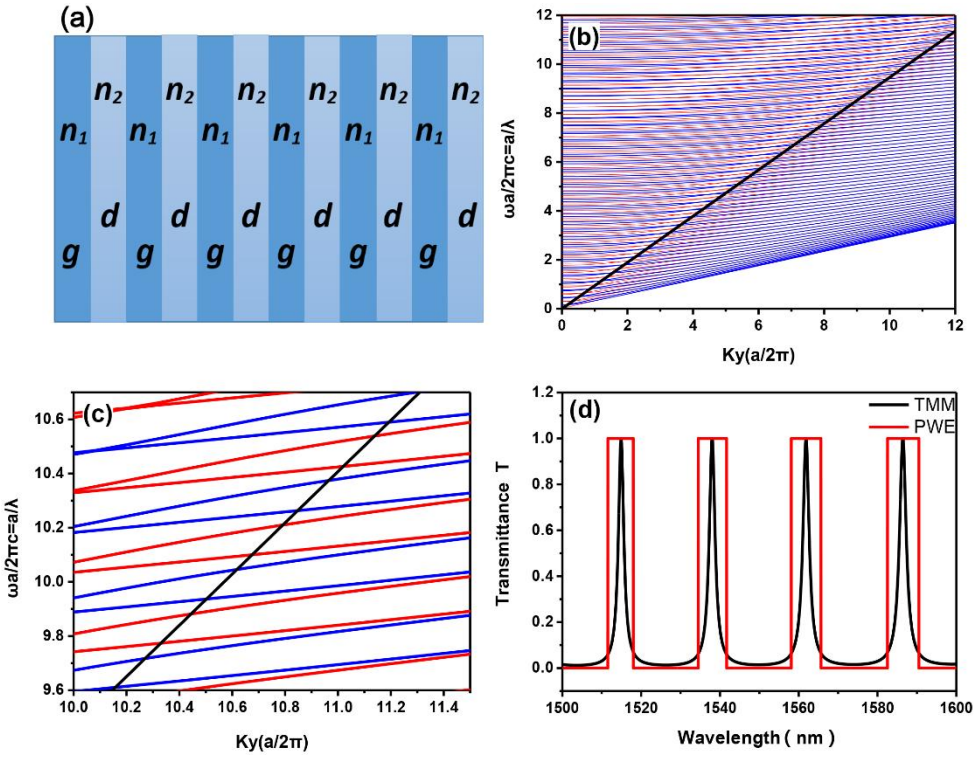

Fig. 6. Corresponding photonic crystals model (a) and band structure (b) for wave vector off-axis *ky*. The close-up view (c) of wavelength ranges from 1500 nm to 1600 nm, the transformed result (d) in accordance with the transmission spectrum obtained by the TMM.

3. Quantum interpretation

In this section, the transmission spectrum of ROTE is derived based on the particle nature of light and regards ROTE as photons going through an optical well. The analogies between wave optics and quantum mechanics possibly open a new door to refresh the view of well-developed classical optics.

3.1 Introduction

As proposed by Zhu [1], an analogy was formed between electron tunneling (quantum tunneling) and photonic tunneling (frustrated total internal reflection, FTIR). Based on this concept, the total reflection is equivalent to an electron encountering a potential step with a larger potential height than its kinetic energy. Moreover, part of the evanescent wave that propagates through a layer of low-RI medium is similar to an electron tunneling through a thin potential barrier. An analogous relationship has been derived from the formal similarity between the Schrödinger equation and Maxwell equations, thus bridging the correspondence between quantum physics and wave optics:

$$\begin{cases} \boldsymbol{E} = \dfrac{\hbar^2 {n_1}^2 \omega^2}{2m_1 {n_2}^2 c^2}\cos^2\theta & (2) \\ \boldsymbol{V_0} = \dfrac{\hbar^2 {n_2}^2 \omega^2}{2m_2 c^2}\left(\dfrac{{n_1}^2}{{n_2}^2}\sin^2\theta + \dfrac{{n_1}^2 m_2}{{n_2}^2 m_1}\cos^2\theta - 1\right) & (3) \end{cases}$$

where E is the kinetic energy of the electron, V_0 is the height of the potential barrier, c is the speed of light in vacuum, $\hbar$ is the reduced Planck constant, m_1 and m_2 denote the effective masses of a particle in different regions, and ω and θ are the angular frequency and the incident angle of light, respectively.

3.2 Potential model setup

The optical model of ROTE (Fig. 7(a)) is converted into the finite potential well of quantum mechanics, as shown in Fig. 7(b). By analogy, quantum potential equations are established independent of the polarization of optical waves. The effective masses are defined in different regions: m_1 for regions *I*, *III*, and *V* and m_2 for regions *II* and *IV*. The boundary conditions for TM and TE waves are achieved by adjusting the ratio of effective masses: $m_2/m_1 = 1/n_2$ for the TM case, and $m_2/m_1 = 1$ for the TE case. The transmission probability of electrons going through a quantum well is well developed according to the classical work by D. K. Ferry [27]. However, in this paper, the details of the derivation also offered for good understanding and further discussion.

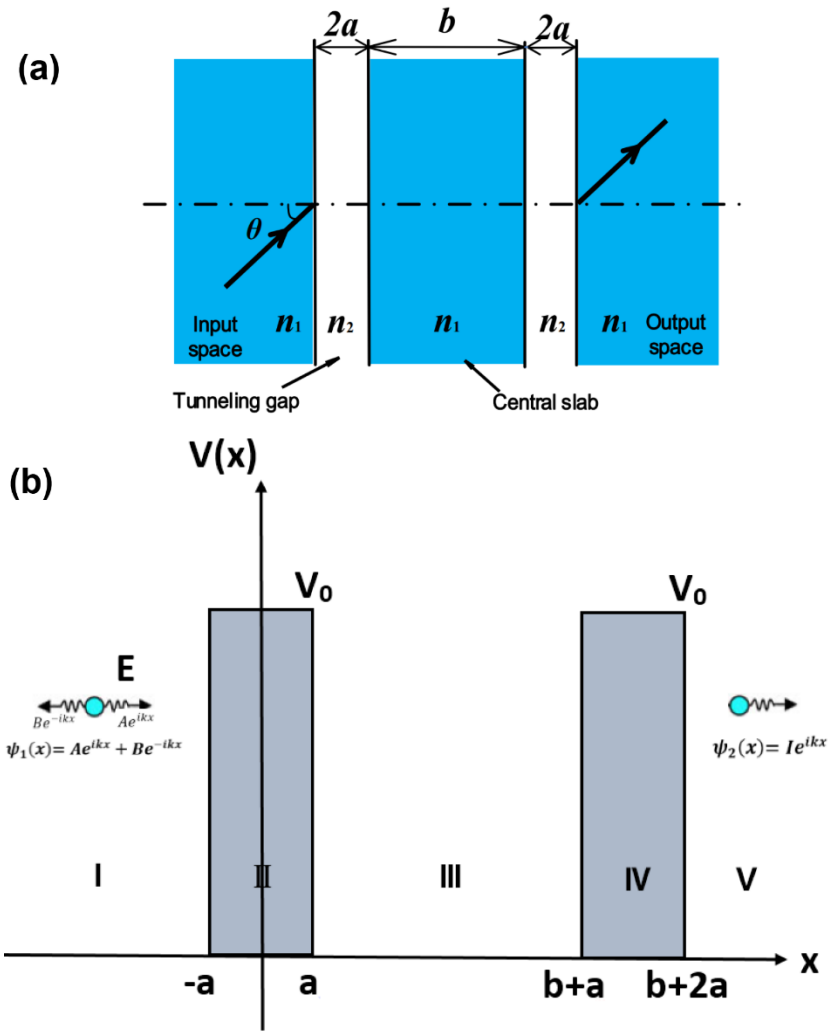

Fig.7. Schematic graph of the ROTE model (a) and corresponding quantum potential model (b).

On both sides of the barriers (in regions *I*, *III*, *and V*), the wave is described by propagating waves, and the wave vector is defined as $k = \sqrt{\frac{2m_1E}{\hbar^2}}$, whereas in the barrier (in regions *II* and *IV*), the wave is attenuated, and the decaying wave vector is defined as $\gamma = \sqrt{\frac{2m_2(V_0-E)}{\hbar^2}}$. Thus, wave function can be defined generally as

$$\psi(x) = \begin{cases} Ae^{ikx} + Be^{-ikx} & x \in region\ I \\ Ce^{i\gamma x} + De^{-i\gamma x} & x \in region\ II \\ Ee^{ikx} + Fe^{-ikx} & x \in region III \end{cases} \quad (4)$$

$$\psi(x) = \begin{cases} E'e^{ikx} + F'e^{-ikx} & x \in region III \\ Ge^{i\gamma x} + He^{-i\gamma x} & x \in region IV \\ Ie^{ikx} + Je^{-ikx} & x \in region\ V \end{cases} \quad (5)$$

where *A* and *B*, *C* and *D*; ..., and *I* and *J* are pairs of forward and backward propagation amplitude coefficient of the wave function, respectively. The boundary conditions are applied by asserting continuity of the wave function and its derivative at each interface. Thus, across the interface *X* = -a, the continuity of these two quantities leads to

$$Ae^{-ikx} + Be^{ikx} = Ce^{-i\gamma x} + De^{i\gamma x} \tag{6}$$

$$ik[Ae^{-ikx} - Be^{ikx}] = \gamma[Ce^{-i\gamma x} + De^{i\gamma x}] \tag{7}$$

Therefore, two of these aforementioned coefficients can be solved in terms of the other two coefficients. Meanwhile, *A* and *B* are solved in terms of *C* and *D*. resulting in the matrix equation,

$$\begin{bmatrix} A \\ B \end{bmatrix} = \begin{bmatrix} (\frac{ik+\gamma}{2ik})e^{(ik-\gamma)a} & (\frac{ik-\gamma}{2ik})e^{(ik+\gamma)a} \\ (\frac{ik-\gamma}{2ik})e^{-(ik+\gamma)a} & (\frac{ik+\gamma}{2ik})e^{-(ik-\gamma)a} \end{bmatrix} \begin{bmatrix} C \\ D \end{bmatrix} \tag{8}$$

Similarly, for every other boundary in the system (from left to right), the matrix equation can be set up based on the continuity of the wave function.

$$\begin{bmatrix} C \\ D \end{bmatrix} = \begin{bmatrix} (\frac{ik+\gamma}{2\gamma})e^{(ik-\gamma)a} & -(\frac{ik-\gamma}{2\gamma})e^{-(ik+\gamma)a} \\ -(\frac{ik-\gamma}{2\gamma})e^{(ik+\gamma)a} & (\frac{ik+\gamma}{2\gamma})e^{-(ik-\gamma)a} \end{bmatrix} \begin{bmatrix} E \\ F \end{bmatrix}$$

$$\begin{bmatrix} E \\ F \end{bmatrix} = \begin{bmatrix} e^{-(ik)(a+b)} & 0 \\ 0 & e^{(ik)(a+b)} \end{bmatrix} \begin{bmatrix} E' \\ F' \end{bmatrix}$$

$$\begin{bmatrix} E' \\ F' \end{bmatrix} = \begin{bmatrix} (\frac{ik+\gamma}{2ik})e^{(ik-\gamma)(a+b)} & (\frac{ik-\gamma}{2ik})e^{(ik+\gamma)(a+b)} \\ (\frac{ik-\gamma}{2ik})e^{-(ik+\gamma)(a+b)} & (\frac{ik+\gamma}{2ik})e^{-(ik-\gamma)(a+b)} \end{bmatrix} \begin{bmatrix} G \\ H \end{bmatrix}$$

$$\begin{bmatrix} G \\ H \end{bmatrix} = \begin{bmatrix} (\frac{ik+\gamma}{2\gamma})e^{(ik-\gamma)(2a+b)} & -(\frac{ik-\gamma}{2\gamma})e^{-(ik+\gamma)(2a+b)} \\ -(\frac{ik-\gamma}{2\gamma})e^{(ik+\gamma)(2a+b)} & (\frac{ik+\gamma}{2\gamma})e^{-(ik-\gamma)(2a+b)} \end{bmatrix} \begin{bmatrix} I \\ J \end{bmatrix} \tag{9}$$

The tunneling effect of electrons from the input side to the output side (from right to left in Fig. 7(b)) is the point of interest; thus, the propagation coefficient *J* is set as 0 (*J*=0) for this purpose. The assumption is that $A = M_{T11} I$, where M_T is the total matrix (i.e., the product of all matrices from right to left). Thus, the transmission probability *T* of the whole ROTE system can be derived as

$$T = \frac{1}{|M_{T11}|^2} \tag{10}$$

However, this solution is complicated and difficult to analyze. To simplify and analyze the solution, the matrix M_L: $\begin{bmatrix} A \\ B \end{bmatrix} = M_L \begin{bmatrix} E \\ F \end{bmatrix}$ is defined for the first barrier from region *I* to *III*. Here, the elements are calculated by the following relations:

$$M_{L11} = \left[\cosh(2\gamma a) - \frac{i}{2}\left(\frac{\frac{m_2}{m_1}k^2 - \frac{m_1}{m_2}\gamma^2}{k\gamma}\right) sinh(2\gamma a)\right] e^{2ika} \tag{11}$$

$$M_{L21} = -\frac{i}{2}\left(\frac{\frac{m_2}{m_1}k^2 + \frac{m_1}{m_2}\gamma^2}{k\gamma}\right) sinh(2\gamma a) \tag{12}$$

$$M_{L22} = M_{L11}^{*} \tag{13}$$

$$M_{L12} = M_{L21}^{*} \tag{14}$$

Similarly, in case of the second barrier, the matrix M_R: $\begin{bmatrix} E' \\ F' \end{bmatrix} = M_R \begin{bmatrix} I \\ J \end{bmatrix}$ is defined from regions *III* to *V*. In addition, M_W: $\begin{bmatrix} E \\ F \end{bmatrix} = M_W \begin{bmatrix} E' \\ F' \end{bmatrix}$, where the subscript indicates the well region *III*. The overall tunneling matrix M_T can be written as

$$M_T = [M_L][M_W][M_R] \tag{15}$$

From this equation, the composite M_{T11} can be expressed as

$$M_{T11} = M_{L11}M_{R11}e^{+ikb} + M_{L12}M_{R21}e^{-ikb} \tag{16}$$

As the two barriers have the same potential height and width, for simplification the remainder of Eq. (11) is written as

$$M_{11} = m_{11}e^{-i\theta} \tag{17}$$

where

$$m_{11} = \sqrt{cosh^2(2\gamma a) + (\frac{\frac{m_2}{m_1}k^2 - \frac{m_1}{m_2}\gamma^2}{2k\gamma})^2 \sinh(2\gamma a)} \tag{18}$$

is the magnitude and

$$\theta = \arctan\left[(\frac{\frac{m_2}{m_1}k^2 - \frac{m_1}{m_2}\gamma^2}{2k\gamma})\tanh(2\gamma a)\right] \tag{19}$$

is the phase of M_{11}. Thus the overall transmission matrix can be offered as

$$|M_{T11}|^2 = 1 + 4|M_{11}|^2|M_{21}|^2\cos^2(kb + \theta) \tag{20}$$

$$T = \frac{1}{|M_{T11}|^2} = \frac{1}{1+4|M_{11}|^2|M_{21}|^2\cos^2(kb+\theta)} \tag{21}$$

3.3 Calculation results and discussion

Fig. 8 illustrates the transmission spectrum of the ROTE structure both in P-pol. and S-pol. The incidence obtained by the quantum model and the optics method (TMM). As observed, for both P-pol. and S-pol., the curves obtained from the quantum model agree well with the results derived using the TMM. Viewed from an overall range (showing the period and free spectral range of the two curves) and the close-up views of a single peak (showing the details of the data), the curves obtained from the different physical models completely overlap. This result demonstrates that the quantum method can successfully solve the transmission spectrum of the ROTE structure.

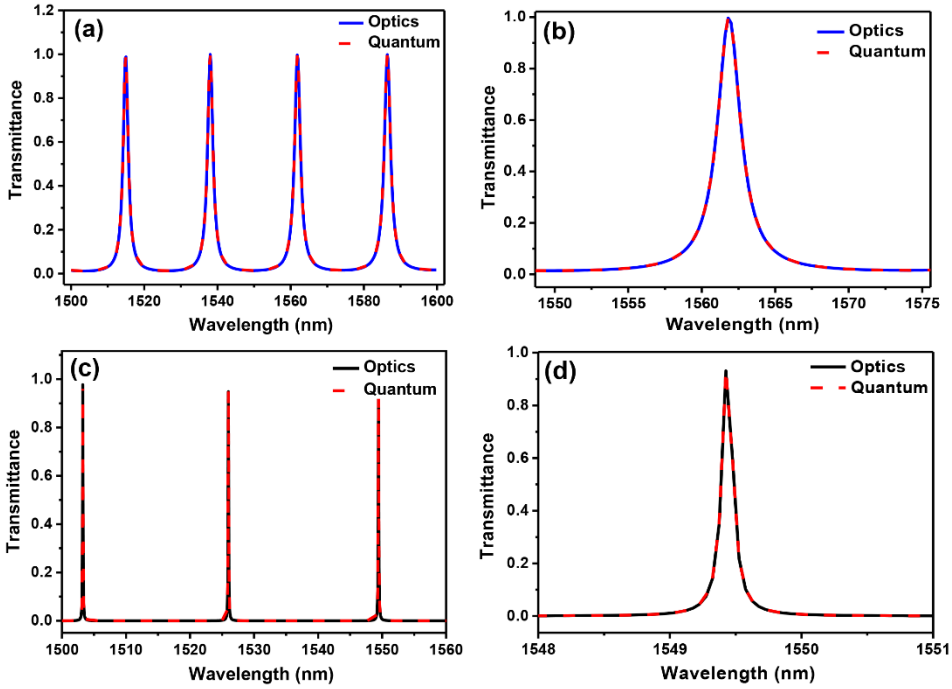

Fig. 8. Transmission spectrum of the ROTE structure with P-polarization ((a) and (b)) and S-polarization ((c) and (d)) obtained using the optics model and the quantum potential model. Generally, the quantum model investigates the dependence of the energy of electrons on system transmittance probability.

The validation of the quantum method has been demonstrated by the correct calculation of the output spectrum of the ROTE structure. Compared with the classical optics model, its special properties are further discussed as follows:

First, the matrix method is involved in both optics model and quantum model, but the core ideas of these two methods are completely different. The production of matrices in the optics model is based on the continuity of the electromagnetic field tangential components; whereas in the quantum method, the boundary conditions are applied in the Schrödinger equation, in accordance with the continuity of the wave function and its derivative at each interface.

Second, optical method needs to deal with two polarization states, and the continuity of the boundary differs for every individual polarization state. Therefore, two sets of equations have to be derived to fit the polarization states of incidence. Meanwhile, in the quantum potential model, the difference in polarization is only reflected in the effective mass ratio in different regions, thus simplifying the complexity of solving process.

Finally, some unprecedented features of ROTE have been revealed by the quantum potential model. Based on Eq. (21), the transmission T reaches maximum when the cosine term in the denominator is equal to 0, that is, it has

$$kb + \theta = (2N + 1)\frac{\pi}{2} \tag{22}$$

here N is a nonnegative integer. For each integer value of N, the corresponding pair of wave vector k and phase value θ can be obtained. The periodicity of the cosine term indicates a series of k and θ values that make maximize transmission. These values of the wave vector correspond to a series of resonant peaks in the transmission spectrum. Eq. (22) provides a direct expression to link the transmission peak positions to the parameters of the ROTE structure (e.g., wavelength, incident angle, dimensions, refractive indices, etc.). It is noted that there is no similar expression that can be obtained using the optical model. However,

based on Figs. 3 and 8, the peak position given by Eq. (22) match those given by the optical modeling and the optical numerical simulation. This is surprising and encouraging. Commonly the quantum analogy is used to explain the optical phenomenon conceptually and qualitatively (e.g., in the photon tunneling), its analysis rarely gives more details than the optical analytical models. The derived Eq. (22) represents the first time that the quantum model can tell more information of the optical systems than the optical models, ever since the proposal of the analogy of photon tunneling and electron tunneling in 1984.

4. Conclusion

In this paper, two methods are applied to analyze the mechanism of the ROTE, one based on wave optics and the other on quantum physics. In the wave optics, the electric field distribution of the ROTE has been simulated by using the FDTD method, and the resonant phenomenon is found to occur at specific wavelengths. Furthermore, optical analysis using the PWE method shows that the ROTE resonant peaks originate from the eigen modes of the corresponding binary muti-layer structure. In quantum physics, the ROTE is represented by the quantum tunneling model that photons tunnel through an optical well with double equal potential barriers. In this model, an implicit function of resonant peak is derived, which indicates that the supported energy states of the ROTE structure are split, and only those photons with proper energies can pass through. The optical-quantum analogical relationship has been verified by the correct calculation of the output spectrum of the ROTE structure, which will benefit the engineering of optical/photonic devices by transplanting the ideas and methods already developed in the quantum physics.

Acknowledgments

This study was financially supported by the National Natural Science Foundation of China (No. 61501316, 61471255, 61474079, 51622507 and 61377068), the Shanxi Provincial Foundation for Returned Scholars (2015-047), 863 project (2015AA042601), Excellent Talents Technology Innovation Program of Shanxi Province (201605D211027), Hundreds of Talents of Shanxi Province, and Research Grants Council of Hong Kong (N_PolyU505/13, 5334/12E, 152184/15E, 509513 and 152127/17E).